Insight Into Carbon Corrosion of Different Carbon Supports for Pt-based Electrocatalysts Using Accelerated Stress Tests in Polymer Electrolyte Fuel Cells

Yongzhen Qi^a, Ying Huang^b, Ziliang Gao^{c,d}, Celine Chen^d, Andrea Perego^{e,d}, Hakan Yildirim^e, Madeleine Odgaard^e, Tristan Asset^d, Plamen Atanassov^{b,d}, Iryna V. Zenyuk^{a,b,d,*}

^aDepartment of Mechanical and Aerospace Engineering, University of California Irvine, Irvine, California, United States of America

^bDepartment of Materials Science and Engineering, University of California Irvine, Irvine, California, United States of America

^cInternational Research Center for Renewable Energy, State Key Laboratory of Multiphase Flow in Power Engineering, Xi'an Jiaotong University, Xi'an, Shaanxi 710049, PR China ^dDepartment of Chemical and Biomolecular Engineering; National Fuel Cell Research Center, University of California Irvine, Irvine, California, United States of America

^eIRD Fuel Cells LLC, 8500 Washington St. NE, Albuquerque, NM 87113, United States *Corresponding author email: irvna.zenyuk@uci.edu

ABSTRACT

Carbon-based catalyst support and Pt catalysts are commonly used in polymer electrolyte fuel cells (PEFCs). During cell start-up and shutdown processes, carbon support oxidation occurs, which leads to losses of electrochemical performance. Here, carbon corrosion accelerated stress tests (ASTs) were performed and lifetimes of high surface area carbon (HSAC) and graphitized carbon (GrC) supports were investigated. 1,000 AST cycles were conducted on Pt/HSAC, while 10,000 AST cycles were conducted on Pt/GrC due to different carbon corrosion rates. Electrochemical surface area (ECSA) loss was found for both Pt/HSAC and Pt/GrC due to Pt loss, Pt detachment and particles coalescence, which also resulted in reduction of SO₃ group coverage and more tortuous H⁺ transport. For Pt/HSAC after 1,000 AST cycles, more than 2 times higher ECSA loss but with only 50% greater particle size growth and similar Pt loss strongly suggested that a greater Pt detachment occurred on HSAC support during the AST cycles. After 1,000 AST cycles, graphitized carbon support was more robust compared to HSAC support, and it showed 2

times less ECSA reduction, 2.5 times less catalyst layer ionic conductivity reduction and 4 times less SO₃ group coverage reduction.

1. Introduction

Polymer electrolyte fuel cells (PEFCs) using hydrogen as a fuel show higher fuel efficiency and decrease in pollutant emissions, which provides a promising way to combat climate change [1]. The major PEFCs applications are developed in the transportation sectors to replace the internal combustion engines (ICEs). Other applications of the PEFCs focus on forklift power sources and electric vehicles range extenders [2,3]. However, due to the high voltage and transient operations, fuel cell lifetime is shortened due to the corrosion mechanisms [4–6], reducing PEFCs vehicles lifetime compared to ICEs. U.S. Department of Energy (DOE) set the lifetime target of 8000 hours, 150000 equivalent driving miles with less than 10% performance loss for light-duty vehicles [7,8]. To meet the lifetime targets, electrochemical characterization and morphology changes resulting from catalysts corrosion and carbon support corrosion must be investigated.

Carbon corrosion occurs within the PEFC catalyst layers that consist of carbon-based support and Pt or Pt- alloy catalysts. It is especially critical at the cathode catalyst layer due to: (i) preferable oxidizing operation condition, (ii) more water participation and Pt catalyzing the carbon corrosion in the operating potential range. The corrosion mechanism of carbon corrosion in the catalyst layer is related to carbon oxidation by water [9,10]:

$$C + 2H_2O \rightarrow CO_2 + 4H^+ + 4e^-, \qquad E_0 = 0.207 V_{RHE}$$
 (1)

Transient startup and shutdown (SUSD) operation usually shows 1.4-1.6 V voltage difference between cathode and anode, which favors the carbon corrosion to occur [11,12]. In addition, H₂

starvation at the anode often leads to cell voltage reversal and, thus, carbon corrosion occurs at the anode [6,13]. Based on the knowledge of these mechanisms, two carbon corrosion accelerated stress test (AST) protocols were developed and recommended by U.S. DOE and the U.S. DRIVE Fuel Cell Tech Team (FCTT). The first AST testing protocol published by U.S. DOE in 2007 consists in having a cathode constant voltage hold of 1.2 V under H₂/N₂ (anode/cathode) atmosphere [14], and the second AST testing protocol published by U.S. DRIVE FCTT in 2013 consists in cell voltage cycling between 1-1.5 V with a sweep rate of 500 mV s⁻¹ under H₂/N₂ (anode/cathode) atmosphere, [15]. However, due to formation of passive oxides during AST, the corrosion rate of the former is 100-150 times slower than that of the latter [10]. Thus, in this work, the 1-1.5 V cycling carbon corrosion AST was used.

Selection of catalyst layer materials and operation conditions are critical to extend the durability of PEFCs. For the carbon support type, despite presenting excellent Pt nanoparticles dispersion, high surface area carbon (HSAC) shows the highest carbon oxidation rate due to the preferential oxidation of the more disordered domains of the carbon support [10,16]. On the other hand, graphitic carbon (GrC) supports show more resistance to electrochemical carbon corrosion with the lowest corrosion rate since it has the greatest graphitic carbon content, which is more robust than disordered amorphous carbon [10,16–19]. Another factor, which impacts carbon corrosion rate is Pt content. It has been shown that Pt catalyzes carbon corrosion in the operation voltage range of 1-1.5 V, most likely via the formation of oxygen- containing surface groups (CO_{ad}) absorbed on the metal surface followed by their oxidation into CO₂ [20,21]:

$$C + H_2O \rightleftharpoons C - O_{ad} + 2H^+ + 2e^-$$
 (2)

$$Pt + H_2O \rightleftharpoons Pt - OH_{ad} + H^+ + e^-$$
 (3)

$$C - O_{ad} + Pt - OH_{ad} \rightleftharpoons Pt + CO_2 + H^+ + e^-$$
 (4)

Pt/HSAC with most disordered amorphous carbon usually shows better Pt dispersion because Pt nanoparticles preferentially deposit within the amorphous domains. However, this also deteriorates carbon support corrosion due to Pt catalyzing carbon corrosion. Apart from material selection, operating conditions also play an important role in carbon corrosion in PEFC. Mittermeier et al. [22] showed the carbon corrosion rate increased with relative humidity (RH). Overall, carbon corrosion in PEFC is still one of the key challenges, thus requiring both an optimization of the catalyst layer design and of the operation conditions to be mitigated.

Carbon corrosion causes irreversible damages to the membrane electrode assembly (MEA). Electrochemical surface area (ECSA) is reduced due to coalescence and sintering of Pt particles [10], as well as, due to collapse of the catalyst layer porous structure [23,24]. Despite many studies focusing on carbon support degradation, only few compared different carbon support types using cycling AST protocol adopted by DOE and it is still unclear how electrochemical performance changes during AST. Macauley et al. [10] focused on carbon support degradation using 1.2 V constant voltage hold, and they estimated significantly different degradation rates for different carbon support types at given cell potential. Hegge et al. [24] studied carbon support degradation after voltage cycling from 1.0-1.5 V at 500 mV/s, and they focused on the changes of catalyst layer porosity and gas diffusivity during carbon corrosion over 1,000 AST cycles. Saha et al. [25] conducted a detailed study on carbon corrosion of HSAC support in PEFC. It showed electrochemical changes during carbon corrosion including ECSA, Pt loading and catalyst layer porosity, etc. However, in their work only one type of carbon support was studied. Few studies give a comprehensive electrochemical characterization comparison between different carbon support types. To better understand the effect of carbon corrosion on different carbon supports, in this work, lifetime of Pt supported on HSAC and GrC supports was

examined, and a detailed electrochemical characterization comparison was performed. Analytical and electrochemical tools were used to quantify the amount of Pt dissolved, resulting loading, catalyst layer thickness, surface groups content and degree of carbon corrosion. Electrochemical measurements were conducted at the beginning of life (BOL), after 100, 500, 1,000, 2500, 5000 and 10,000 AST cycles to assess polarization behavior, ECSA, etc. along with an extensive array of physicochemical and microscopic characterization methods, aiming to provide a complete picture of the changes undergone by the different catalytic layers during the AST.

2. Materials and methods

2.1. Material preparation.

Catalyst inks and MEAs were custom-made by IRD Fuel Cells (Albuquerque, NM, United States) for the purpose of this study, and the ink formulation and preparation are in accordance with best industrial practices. For all membrane electrode assemblies (MEAs), PFSA membranes with thickness of 18 µm were used. The anodes for all MEAs were loaded with 0.15 mg cm⁻² of Pt while the cathodes had Pt loading of around 0.53 mg cm⁻² and 0.648 mg cm⁻² for Pt/HSAC and Pt/GrC, respectively. Pt loading discrepancy between these two samples is due to difficulty of achieving the same Pt loadings during the manufacturing process given the supports are different. In this work, Pt/HSAC and GrC supports were used on cathode sides as different carbon supports and a detailed electrochemical characterizations comparison was conducted. Two MEAs with each carbon support were investigated to ensure the reproducibility of the study.

2.1.1. Cell assembly.

A 5 cm x 5 cm Freudenberg H23C6 with micro porous layer (MPL) was used as the gas diffusion layer (GDL). A 50 cm² 14 channel serpentine flow-field with channel and land width of 0.5 mm x 0.5 mm was used as flow-field. Cell active area was controlled as 25 cm² and a 5.5 cm x 5.5 cm Teflon fiberglass sheet layer of 180 μm thickness on both sides between the MEA and the bipolar plate as hard-stop gasket was used to achieve a 20% compression of the GDL.

2.2. In Situ Electrochemical Diagnostics.

All the experiments were done using a Biologic VSP potentiostat and a Scribner 850e fuel cell hardware. Cells first were activated by conducting voltage cycling break-in followed by voltage recovery process to hydrate the catalyst layer and to remove the contaminants.

Electrochemical characterization was performed after the activation process, as described below.

2.2.1. Cell voltage break-in and recovery.

A cell break-in process was performed by using 0.8/1.5 standard liter per minute (SLPM) ultrahigh purity (UHP) H₂ and compressed air at anode and cathode, respectively at 80 °C and 100% RH with an absolute backpressure of 150 kPa. A series of constant voltage holds with 200 repeated cycles were performed by applying constant voltages to the cells at 0.8 V, 0.5 V and 0.2 V for 30 seconds, respectively.

During voltage recovery the cell was held at 0.1 V for 7200 seconds using 0.45/0.25 SLPM UHP H₂ and air at the anode and cathode, respectively at 40 °C and 150% RH with an absolute backpressure of 150 kPa. Previous study showed recovery process was an effective way to remove the surface contaminants and increased the electrochemical surface area (ECSA) [26].

2.2.2. Carbon corrosion accelerated stress test.

Carbon corrosion ASTs for PEMFC components were performed using the protocol published by U.S. DRIVE FCTT in 2013 [15]. Briefly, the potential was cycled between 1 and 1.5 V at 500 mV s⁻¹ with a triangular wave pattern. Cell temperature was 80 °C under fully humidified H_2/N_2 flow.

2.2.3. H_2/Air polarization curves.

The polarization curve measurements were performed in galvanostatic mode, on the anodic direction from 2 to 0 A cm⁻² (2, 1.8, 1.6, 1.4, 1.2, 1.0, 0.8, 0.6, 0.4, 0.2, 0.1, 0.08, 0.04, 0.02, 0 A cm⁻²). at 80 °C, 100% RH with an absolute backpressure of 150 kPa. Each step of the polarization curve was held for 180 s. The polarization curve measurements were conducted in anodic direction with the reactant gas stoichiometry factors of 2/2 at the anode/cathode, respectively. During the polarization curve measurements, high frequency resistance (HFR) was measured under the same operating condition using a built- in function of the potentiostat, which performs a single point impedance calculation at 1 kHz.

2.2.4. Cyclic voltammetry.

The cell was humidified by purging 0.5/0.5 SLPM pure N₂ without back pressure at 60 °C and 100% RH for 1 hour. A cathode surface cleaning step was performed by conducting a repeated cyclic voltammetry (CV) under 0.2/0.3 SLPM H₂/N₂ with a voltage range of 0.05 V to 1.05 V at 200 mV s⁻¹ scan rate for 30 cycles. Subsequently, CV measurements with 100 mV s⁻¹ and the same voltage range and same gas flow rates were conducted.

2.2.5. CO displacement and CO stripping methods.

Prior to CO displacement, a surface cleaning CV step of 20 cycles using 1/1 SLPM of 5% H₂ on anode and pure N₂ on cathode was performed. After that, the cell was held at 0.4 V for 7 min without any changes of gas composition and gas flow rates. This was first followed by a 2 min N₂ purge at the cathode, after what the gas was instantly switched to 2% CO. The cell was then held under the same constant voltage with 2% CO gas purging continuing for 5 min to establish another constant current baseline. Because of the residual air gas within the system, the first CO displacement measurement was contaminated by the ORR. Hence the result of the first measurement was discarded. After that, CO displacement experiments were conducted from 0.1 V to 0.4 V in increments of 0.1 V. After CO displacement, 1 SLPM pure N₂ was purged at cathode side for 20 min to remove the residual CO gas in the cell. Subsequently, a CV under 1/1 SLPM 5% H₂ and N₂ with a potential sweep range from 0.05 V to 1.05 V at 40 mV s⁻¹ scan rate was performed and repeated 5 times.

2.2.6. Electrochemical impedance spectroscopy (EIS) method.

The cell was held at 0.2 V for 5 min using 0.2/0.3 SLPM of pure H₂ on anode and pure N₂ on cathode without back pressure at 60 °C and 100% RH. Subsequently, a 10 mV AC potential was applied to the cell over a frequency range from 500 kHz to 100 mHz with 8 points per decade recording rate. EIS measurements were repeated twice to provide reproducibility.

For Pt/HSAC, the aforementioned electrochemical characterization was performed for beginning of life (BOL), after 100 AST cycles, after 500 AST cycles and after 1,000 AST cycles, which was considered as the end of life (EOL) for the cell. For Pt/GrC, due to lower carbon corrosion rate [20], more AST cycles were performed. Electrochemical characterization was

performed for beginning of life (BOL), after 100, 500, 1,000, 2500, 5000 and 10,000 AST cycles, which was considered as the EOL of the cell.

2.3. Ex Situ Electrochemical Diagnostics.

2.3.1. Scanning electron microscope (SEM) sample preparation and imaging.

Cross-sectional MEA samples using HSAC and GrC supports were embedded in epoxy resin, polished and imaged with a FEI Magellan 400 scanning electron microscope detector operating at 3.00 kV accelerating voltage. SEM measurements were repeated for BOL and EOL for each carbon support type, and catalyst layer thicknesses were measured from the SEM micrographs.

2.3.2. Scanning transmission electron microscopy (STEM).

At BOL, a JEOL Grand ARM300F microscope, equipped with two spherical aberration correctors, was used to perform the aberration-corrected scanning transmission electron microscopy (AC-STEM) characterization for both Pt/HSAC and Pt/GrC MEAs. The TEM imaging was performed at 300 kV.

2.3.3. Transmission electron microscopy (TEM).

After AST, the catalyst layers were scraped from the MEA to make powders. The powders were then dispersed in ethanol by sonication. A few drops of the suspension were deposited onto holey carbon-coated copper grids. The images were obtained using a JEOL JEM-2800 microscope at 200 kV.

2.3.4. Particle size analysis.

The TEM images were processed with Fiji ImageJ [27] using thresholding and the ROI manager. The overlapped particles were removed. The particles were converted into solid ellipses after the processing. The measure function of Fiji Image J provides the length of the major and minor axis of the ellipses. The particle size was calculated by taking the square root of the product of the length of major and minor axis. TEM is a good way to show the morphological change of the particle. However, TEM only provides the particle size distribution in a small field of view (usually less than 100 nm × 100 nm). Also, the particle size might be overestimated if the overlapping particles were not removed and has a large uncertainty depending on how the thresholding was done. To decrease the uncertainty, ROI manager was used to remove the overlapping particles and thresholding value was carefully chosen based on the grayscale histogram of each image.

2.3.5. *Identical location* μ -*X-ray Fluorescence (XRF)*.

To ensure identical locations were mapped before and after the AST, a 25- μ m PTFE template was prepared, and, using the MEA as a reference, a hole was cut out in the template near the center of the active area. The diameter of the hole was the same as the diagonal of a 2048 μ m by 2048 μ m area. Ex situ μ -XRF measurements were performed using the XGT-9000 Horiba XRF microscope. A focus distance of 1 mm and a 10 μ m capillary with 1024 pixels in both x and y directions were used to map an area of 2048 μ m by 2048 μ m, resulting in a resolution of 2 μ m × 2 μ m. The x-ray energy was 50 keV, and the reflected x-ray signal to the detector included Pt contribution from both the anode and the cathode as the x-ray penetrates through the entire MEA. Therefore, the total average Pt loading is the sum of anode and cathode loadings, and it was quantified using a calibration curve generated from 10 μ m capillary maps of samples with

known Pt loading. 2D colormaps were generated in MATLAB using the quantified total average Pt loading and raw fluorescence images from the microscope.

2.3.6. X-ray photoelectron spectroscopy (XPS).

The GDL of the MEA was removed. The sample was mounted on the sample loader and the cathode side was facing up. The XPS measurement was conducted on the cathode side of the MEA. XPS was performed on a Kratos AXIS Supra spectrometer with a monochromatic Al Kα source. CasaXPS software was used to analyze the data. The fitting was based on our previous calculations and publications [28,29]. For the C *Is*, a linear substation was used. The graphitic C spectra were fitted with an asymmetric modified 20% Gaussian/80% Lorentzian line shape, and other spectra were fitted with a 70% Gaussian/30% Lorentzian line shape. For the Pt *4f*, a Shirley substation was used, and all spectra were fitted with an asymmetric modified 70% Gaussian/30% Lorentzian line shape.

2.3.7. Raman spectroscopy.

All Raman spectra were obtained using a Horiba LabRAM-HR Evolution Confocal Raman Microscope at 633 nm laser with a 100x objective and a 600 g/mm grating. Twenty individual 30s spectra were summed.

2.3.8. X-ray diffraction (XRD).

XRD patterns were collected on a Rigaku Ultima III X-Ray Diffractometer with a Cu K α X-ray generator. PDXL software was used to analyze the data. Measurement was conducted on the

MEA with cathode facing up. The crystalline sizes of the samples were calculated by applying whole powder pattern fitting method after the phase identification.

2.4. Calculation methods.

2.4.1. Double layer capacity.

Double layer capacity ($C_{\rm dl}$) is considered as the capacity summation of the four different interfaces within the catalyst layer: (i) Pt/ionomer, (ii) Pt/water, (iii) carbon/ionomer and (iv) carbon/water [30]. Investigating $C_{\rm dl}$ change during the carbon corrosion AST provides more insights on interfacial properties change between solid/ionic phase materials. In this work, $C_{\rm dl}$ was calculated using the following equation:

$$I = C_{\rm dl} \times \frac{\rm dV}{\rm dt} \tag{5}$$

where I denotes the upper/lower current in the double layer region (0.4-0.5 V) from CV measurements. $\frac{dV}{dt}$ represents the voltage sweep rate of CV measurement, here 100 mV s⁻¹.

2.4.2. Effective ionic conductivity.

Effective ionic conductivity was derived by using a H₂/N₂ EIS fitting model based on Qi et al.'s work [31]. The model is based on Obermaier et al.'s model [32], which modeled the equivalent circuit of catalyst layer based on transmission line model. In this work, catalyst layer ionic conductivity was derived by inputting the frequency, cell active area, catalyst layer thickness, imaginary impedance and real impedance etc. into the fitting model.

2.4.3. CO displacement charge.

During CO displacement technique, CO bonds onto Pt, leading to the displacement of adsorbed ion species at the Pt surface, for example H⁺ and SO₃⁻ groups, which results in charge transfer and current flow. According to Equation (6), negative current signal was recorded when constant cell potential, which was greater than the potential of zero charge (PZC) of Pt was applied. CO displacement charge was the integration of CO displacement peak in the current-time plot.

$$Pt - An + CO + e^- \rightarrow Pt - CO + An^-$$
 (6)

where Pt-An is anion adsorbed on Pt surface. Here at 0.4 V SO₃ group of ionomer is absorbed anion species, which follows conventions of Qi et al. [33] and Garrick et al. [34].

2.4.4. CO stripping charge.

CO stripping charge was calculated by integrating the CO stripping peak from CO stripping measurements then divided by the scan rate of 40 mV s⁻¹. The CO stripping mechanism is a multiple steps process that includes, for example, the formations of OH_{ads} and COOH_{ads}, which followed Langmuir-Hinshelwood mechanism [35]:

$$H_2O + * \leftrightarrow OH_{ads} + H^+ + e^- \tag{7}$$

$$CO_{ads} + OH_{ads} \rightarrow COOH_{ads}$$
 (8)

$$COOH_{ads} \rightarrow CO_2 + H^+ + e^- + *$$
 (9)

where * denotes the free surface site.

2.4.5. Electrochemical surface area.

Electrochemical surface area (ECSA) was calculated from the H_2 under potential deposition ($H_{\rm upd}$) region of CV:

$$ECSA_{H_{upd}} (m^2 g^{-1}) = \frac{Q_{H_{upd}}(C)}{210 \frac{\mu C}{cm^2} \times Area (cm^2) \times L_{pt} (\frac{mg}{cm^2})} \times 10^5$$
 (10)

where $Q_{H_{upd}}$ (C) is charge integration over the H_{upd} region and area (cm²) denotes the cell active area. L_{pt} denotes the Pt loading (mg cm⁻²). 210 $\frac{\mu C}{cm^2}$ is the charges per H_{upd} monolayer [36].

2.4.6. SO_3^- -group coverage.

SO₃ group coverage was calculated using the following equation [34]:

$$\theta_{SO_3^-} = \frac{2 \times q_{dis}}{q_{strip}} \times 100\% \tag{11}$$

where q_{dis} is the CO displacement charge, q_{strip} denotes the CO stripping charge. There is a multiplier 2 in the numerator since CO requires two electrons to oxidize CO to CO₂. The coverage is an averaged and the SO_3^- group coverage corresponds to an average ratio of Pt atoms that are covered by SO_3^- groups over all electrochemically active Pt atoms.

3. Results and discussion

3.1. Polarization curves, voltage performance and HFRs.

Fig. 1a shows the polarization curves of MEA with Pt/HSAC support over the duration of 1,000 carbon corrosion AST cycles. After 100 AST cycles, Pt/HSAC showed a slight loss in performance compared to the BOL, with a voltage loss of 54 mV at 1 A cm⁻² from 0.644 V to 0.59 V (Fig. 1b). From HFR results shown in Fig. 1a, after 100 AST cycles, the HFR of the cell decreased from 56.4 mohms cm² to 53.9 mohms cm² due to the better contacts between GDL/catalyst layer and catalyst layer hydration. After 500 AST cycles, a significant performance loss was shown in Fig. 1a. However, a similar HFR of the cell of 55.9 mohms cm² was measured after 500 AST cycles (Fig. 1a), which indicates that the performance drop might be due to loss of the ECSA or due to the collapse of the catalyst layer porous structure leading to a mass transport problem, but not due

to intrinsic losses in the ionic/electronic conductivity. At the EOL, the performance loss further deteriorated to 0.247 V at 0.2 A cm⁻² (Fig. 1a). In addition, the HFR increased to 73.3 mohms cm² (30% increase compared to BOL), this being likely induced by contact loss between catalyst layer and the GDL, which indicates that at the EOL, the cell had both ohmic and mass transport issues leading to significant loss of performance.

Cell performance drop for Pt/GrC was much more moderate since graphitized carbon support is more robust. From the results shown in Fig. 1c, cell performance deteriorated 14 mV after 1,000 AST cycles and voltage at 1 A cm⁻² was 0.656 V (Fig. 1d). HFR shown in Fig. 1c after 1,000 AST cycles decreased from 52.8 mohms cm² to 50.8 mohms cm² compared to BOL due to the better contacts at GDL/catalyst layer interfaces and further hydration of the catalyst layer, which is similar to what was observed for Pt/HSAC. Cell performance maintained after 2500 AST cycles and a 1 mV voltage decrease was found. After 5000 AST cycles, the cell degraded and a voltage loss of 63 mV at 1 A cm⁻² was observed compared to BOL (Fig. 1c and Fig. 1d). Apart from that, Pt/GrC MEA experienced voltage loss of 69 mV at 0.8 A cm⁻² and 129 mV at 1.5 A cm⁻², which did not meet the DOE target of 40 mV loss at 0.8 A cm⁻² and 40 mV loss at 1.5 A cm⁻² [7]. The performance decreased significantly at the EOL shown in Fig. 1c, which was after 10,000 AST cycles. Cell voltage decreased to 0.561 V at 0.2 A cm⁻² at the EOL due to the loss of ECSA and porous structure collapse of catalyst layer. However, in Fig. 1c, HFR remained constant during the AST, which indicates the contacts between catalyst layers and GDLs remains mostly intact.

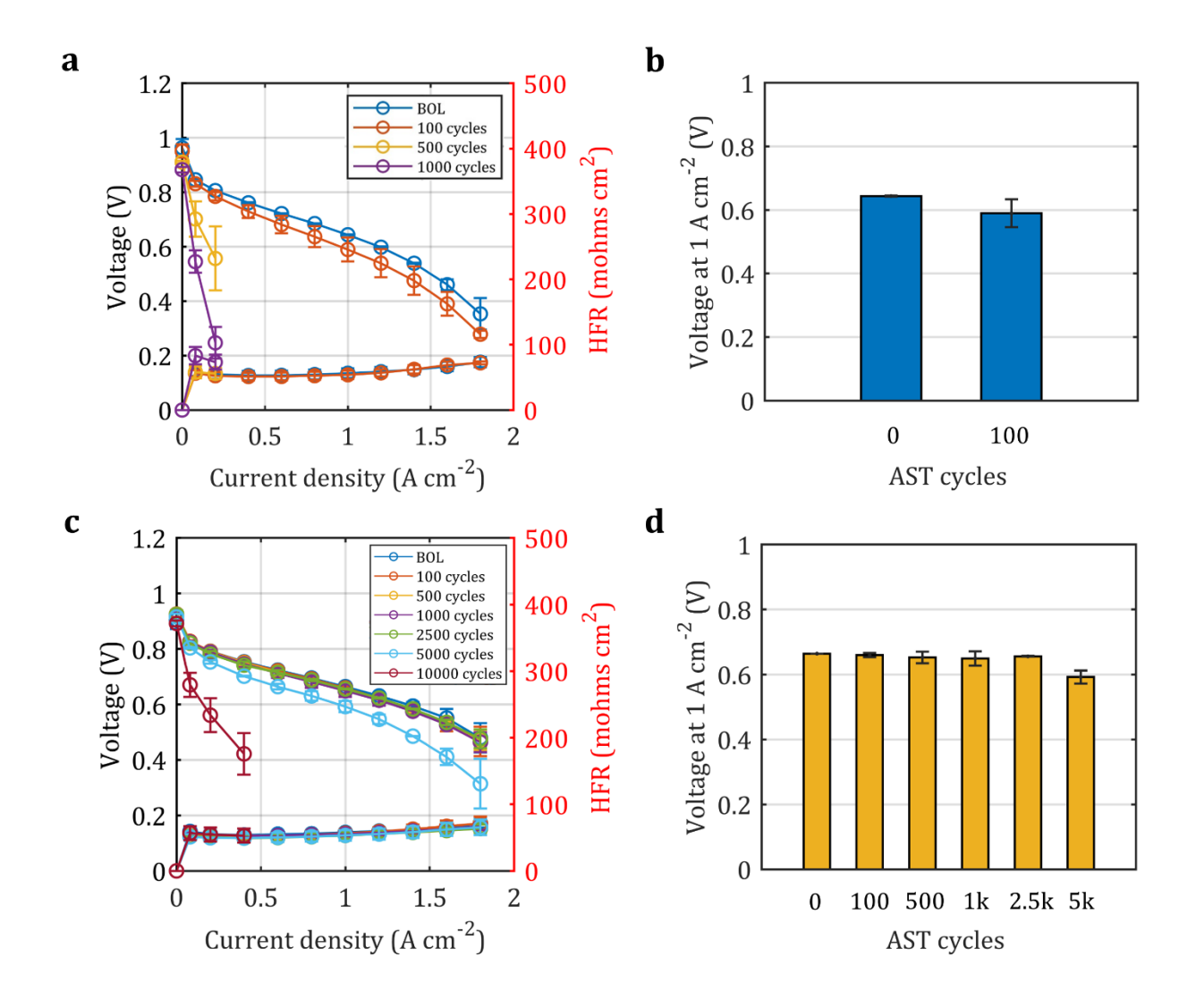


Fig. 1. Performance and HFRs of MEAs using HSAC (a and b) and GrC (c and d) support during carbon corrosion AST. For Pt/HSAC, (a) MEA performance at 80 °C, 100% RH, 150 kPa in H₂/Air with stoichiometric anode and cathode flows of 2 and 2 and HFR at BOL, after 100, 500, and 1,000 AST cycles (EOL), (b) voltage at 1 A cm⁻². For Pt/GrC, (c) MEA performance at 80 °C, 100% RH, 150 kPa in H₂/Air with stoichiometric anode and cathode flows of 2 and 2 and HFR at BOL, after 100, 500, 1,000, 2500, 5000, and 10,000 AST cycles (EOL), (d) voltage at 1 A cm⁻².

3.2. Cathode catalyst layer thicknesses.

Averaged cathode catalyst layer thicknesses at BOL and EOL for Pt/HSAC and Pt/GrC are shown in Fig. 2c and Fig. 2f, respectively according to the cross-section SEM measurement

results for Pt/HSAC and Pt/GrC at BOL and EOL (Fig. 2a, Fig. 2b, Fig. 2d and Fig. 2e). Cathode catalyst layer thickness of Pt/HSAC decreased from 11.4 μm at BOL (Fig. 2a) to 3.7 μm after 1,000 AST cycles at EOL (Fig. 2b). For Pt/GrC, thickness of cathode catalyst layer decreased from 18.7 μm at BOL (Fig. 2d) to 5.91 μm after 10,000 AST cycles at EOL (Fig. 2e). Thickness reduction for Pt/HSAC due to the carbon support oxidation also explained the increase of HFR (Fig. 1a). At EOL, HFR for Pt/HSAC increased 30% due to the reduction of catalyst layer thickness, which resulted in insufficient contacts between GDL and catalyst layer. However, for Pt/GrC, even though catalyst layer thickness decreased to 5.91 μm at EOL, it still provided sufficient contacts at the catalyst layer/GDL interface, which resulted in a maintained HFR (Fig. 1c).

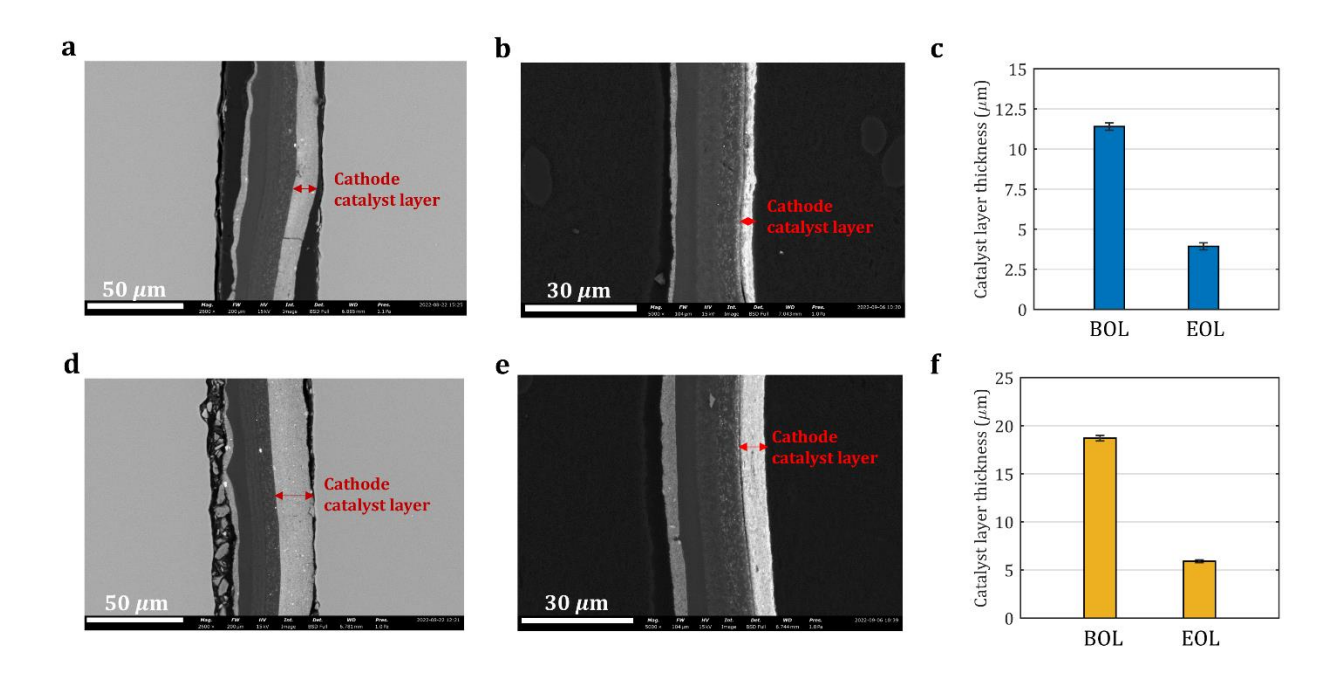


Fig. 2. Cross-sectional scanning electron microscope (SEM) and averaged cathode catalyst layer thickness reductions for Pt/HSAC (a-c) and Pt/GrC (d-f) during AST. Cathode catalyst layer thicknesses for Pt/HSAC using SEM at (a) BOL and (b) EOL. (c) Thickness reduction at EOL for Pt/HSAC. Catalyst layer thicknesses for Pt/GrC using SEM at (d) BOL and (e) EOL. (f) Thickness reduction at EOL for Pt/GrC.

3.3. Cathode double layer capacities, CV measurements and ECSAs.

Catalyst layer and interfacial properties were measured for MEAs with both HSAC and GrC supports during AST. For Pt/HSAC, Cdl was measured using the Equation (5) and shown in Fig. 3a. According to Iden and Ohma's work [30], C_{dl} was determined as the summation of four interfaces within the catalyst layer, which are Pt/ionomer, Pt/water, carbon/ionomer, and carbon/water. At BOL, Pt/HSAC shows a much higher C_{dl} of 119.6 mF cm⁻² (Fig. 3a) compared to the 37.8 mF cm⁻² of Pt/GrC (Fig. 3c) because of the greater surface area of carbon black support due to the internal porous structure (amorphous domain) [34]. C_{dl} for Pt/HSAC increased to 152.2 mF cm⁻² after 100 AST cycles and further increased to 158.3 mF cm⁻² after 500 AST cycles because the carbon corrosion led to a roughening of the carbon surface, and thus a higher surface area was exposed to ionomer and water. At EOL, C_{dl} decreased to 128.6 mF cm⁻², indicating, a collapse of the porous network and thus, a decrease accessibility of the carbon support to ionomer/water. A total capacity increase of 9 mF cm⁻² (7.5%) at EOL was shown in Fig. 3a. For Pt/GrC, C_{dl} shown in Fig. 3c remained at around 37.4 mF cm⁻² after 100 AST cycles, followed by a gradual increase with the AST cycling number. Eventually a significant increase of 26.8 mF cm⁻² (69.8%) at EOL was observed, reaching 64.2 mF cm⁻². The increase of C_{dl} for Pt/GrC was much greater than that of Pt/HSAC, as the oxidation of the ordered graphitic carbon logically resulted in the creation of a more amorphous, porous and disorganized carbon surface, leading to a significant C_{dl} increase compared to Pt/HSAC.

Fig. S1 show the CV measurements for Pt/HSAC and Pt/GrC during AST, respectively. H_{upd} peaks decreased as a function of cycle number, as expected for both HSAC and GrC supports. The decrease of H_{upd} peak for Pt/GrC was much smaller compared to Pt/HSAC because Pt/HSAC had

higher carbon oxidation rate at amorphous domains where Pt particles were well dispersed and catalyzed carbon corrosion reaction. ECSA results calculated from $\boldsymbol{H}_{\text{upd}}$ peaks for both carbon support types are shown in Fig. 3b and Fig. 3d. Reductions of ECSAs show consistency with the decrease of $H_{\rm upd}$ peaks. Pt/HSAC, at the BOL showed higher ECSA value of 43.5 m² g⁻¹ (Fig. 3b) compared to 26.2 m² g⁻¹ for Pt/GrC (Fig. 3d) because of better Pt dispersion within the internal porous carbon structure. ECSA for Pt/HSAC (Fig. 3b) decreased most rapidly at first 100 AST cycles from 43.5 m² g⁻¹ to 36.2 m² g⁻¹, then slightly decreased to 24.7 m² g⁻¹ (41.8%) after 500 AST cycles. Eventually, ECSA decreased to 20.7 m² g⁻¹ and a total ECSA loss of 22.8 m² g⁻¹ (52.4%) was observed for Pt/HSAC at the EOL. For Pt/GrC (Fig. 3d), reduction of the ECSA was much more moderate due to protective carbon support. ECSA remained constant after the first 100 AST cycles and was reduced by 4.23 m² g⁻¹ (16.1%) after the first 1,000 AST cycles, then followed by a decrease of 8.03 m² g⁻¹ (30.6%) after 5,000 AST cycles, which met DOE target of a 40% loss of initial surface area after 5,000 AST cycles [7]. Eventually, ECSA for Pt/GrC decreased by 44% and reached 14.7 m² g⁻¹ after 10,000 AST cycles (EOL). ECSA was also calculated and summarized using CO stripping method for both Pt/HSAC and Pt/GrC after certain AST cycles in Fig. S2, and it showed good consistency compared to using $H_{\rm upd}$ charge integration. At BOL shown in Fig. S2a, it shows 45.6 m² g⁻¹ ECSA for Pt/HSAC and 28.4 m² g⁻¹ for Pt/GrC respectively. For Pt/HSAC at EOL, Fig. S2a shows the calculated ECSA of 17.7 m² g⁻¹ using CO stripping method, which is close to 20.7 m² g⁻¹ using H_{upd} charge integration. For Pt/GrC, after 1,000 AST cycles, ECSA was 25.8 m² g⁻¹ using CO stripping method, compared to 22 m² g⁻¹ using H_{upd} charge integration (Fig. S2b). After 10,000 AST cycles, it shows 11.1 m² g⁻¹ ECSA using CO stripping method, compared to 14.7 m² g⁻¹ using H_{und} charge integration. Possible reasons for ECSA reduction might be: i) Pt nanoparticles detachment due to carbon corrosion, ii)

Pt dissolution during the AST as Pt^{2+} , iii) Pt nanoparticles growth due to 2D/3D Ostwald ripening and coalescence, and iv) burying of the Pt nanoparticles during the catalyst layer structural collapse and the resulting loss in H^+/O_2 accessibility. Reduction of the ECSA also partially explains the performance decrease shown in Fig. 1a and Fig. 1c for Pt/HSAC and Pt/GrC, respectively.

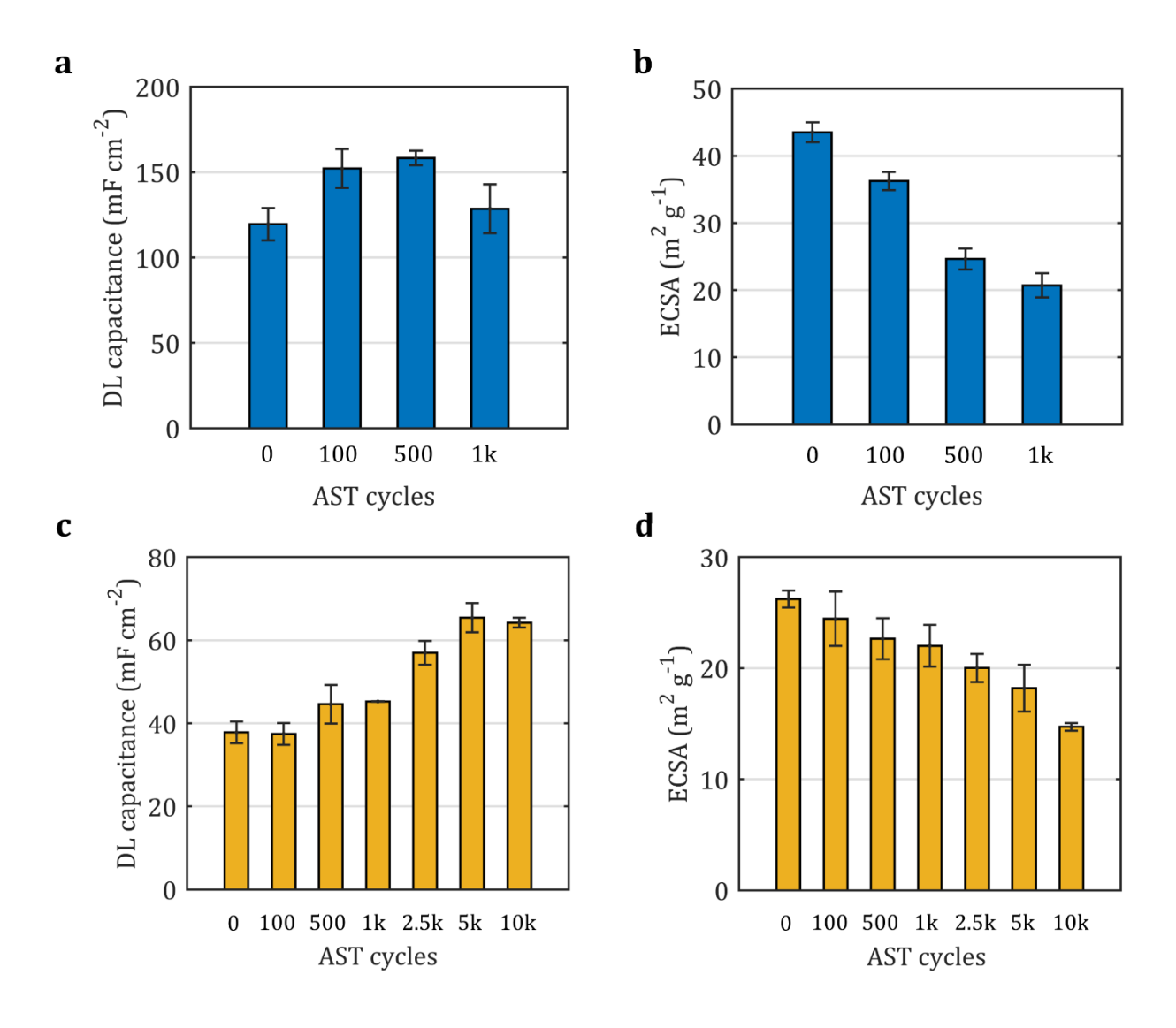


Fig. 3. Double layer capacitance, CV measurements and ECSAs of MEAs using HSAC (a-b) and GrC (c-d) supports during carbon corrosion AST. For Pt/HSAC, (a) cathode double layer capacitance, (b) cathode ECSA at BOL, after 100, 500, and 1000 AST cycles (EOL). For Pt/GrC, (c) cathode double layer capacitance, (d) cathode ECSA at BOL, after 100, 500, 1000, 2500, 5000, and 10000 AST cycles (EOL).

3.4. Cumulative average Pt loading maps.

Local averaged Pt loading distributions at the BOL and EOL for Pt/HSAC and Pt/GrC are shown in Fig. 4c and Fig. 4f, respectively according to identical location micro XRF maps for BOL (Fig. 4a and Fig. 4d) and EOL (Fig. 4b and Fig. 4e). Again, in this work, the X-rays penetrate both the anode and cathode catalyst layer and therefore the cumulative average Pt loading of both anode and cathode were shown. Fig. 4c shows that average Pt loading of Pt/HSAC reached 0.675 mg cm⁻² at the BOL (Fig. 4a) and decreased to 0.577 mg cm⁻² at the EOL (Fig. 4b). For Pt/GrC, averaged Pt loading shown in Fig. 4f decreased from 0.798 mg cm⁻² at BOL (Fig. 4d) to 0.732 mg cm⁻² at EOL (Fig. 4e). Pt loss for Pt/GrC after 10,000 AST cycles was similar compared to that loss for Pt/HSAC after 1,000 AST cycles, which again indicating graphitized carbon support is much more robust and protective. For both Pt/HSAC and Pt/GrC, cumulative averaged Pt loadings decreased at their EOLs, which indicates that Pt loss might be one of the reasons causing the reduction of ECSA.

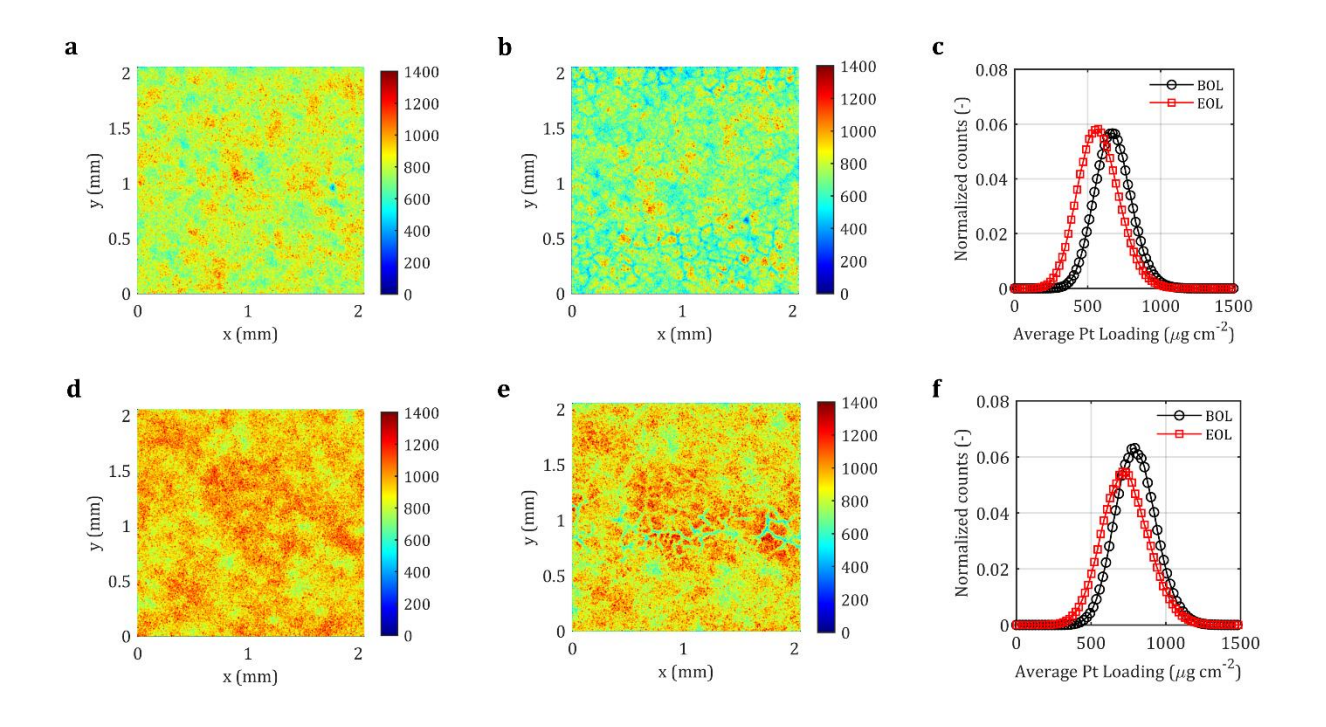


Fig. 4. Identical location micro X-ray fluorescence (XRF) maps for Pt/HSAC at (a) BOL and (b) EOL. (c) Loading-frequency distribution for Pt/HSAC at BOL and EOL. Identical location micro X-ray fluorescence (micro XRF) maps for Pt/GrC at (d) BOL and (e) EOL. (f) Loading-frequency distribution for Pt/GrC at BOL and EOL.

3.5. Cathode Pt particle sizes.

Cathode side Pt particle sizes for Pt/HSAC and Pt/GrC at BOL and after certain AST cycles were determined by TEM/STEM and XRD (Fig. S3-S4) and summarized in Fig. 5. The Pt particle sizes increased after AST in both samples, which is due to the Pt particle coalescence and sintering. Based on TEM/STEM results shown in Fig. 5a, the average Pt sizes of Pt/HSAC increased from 2.25 nm at BOL to 3.96 nm after 1,000 AST at EOL. The average Pt sizes of Pt/GrC raised from 2.25 nm at BOL to 8.27 nm after 10,000 AST cycles at EOL. The TEM/STEM data also provide particle size distributions and reveal the morphological changes of the Pt particles (Fig. S3). After certain AST cycles, the Pt particles in the Pt/GrC at EOL demonstrated a dumbbell-like shape. As comparison, the particle shapes in Pt/HSAC at EOL are

closer to spheres, which are more similar to the Pt in pristine samples. XRD measurement results (Fig. S4, Table. S1 and Table. S2) were summarized in Fig. 5b, and it shows Pt particle size increased from 2.5 nm to 4.2 nm (68%) after 1,000 AST cycles at EOL for Pt/HSAC, while for Pt/GrC Pt particle size grew from 3.4 nm to 5.4 nm (59%) after 10,000 AST cycles at its EOL.

Overall, the average particle sizes gained by whole powder pattern fitting based on XRD results are in good alignment with the ones gained from TEM/STEM (Fig. 5d). However, the difference between the sizes gained different measurements were larger when the Pt sizes are bigger. This is because of the difference between these measurements. EM is detecting the size of Pt particles individually based on the morphology images of a small field of view. The average size is calculated with an assumption that the particles were in ellipse shape. XRD is measuring the diffraction of the whole samples and provides the crystalline sizes. In our case, the diffraction pattern of the Pt might be affected by the amorphous carbon inside the sample [37]. Also, in the Pt/GrC at EOL, there is a high probability that most of the crystallites aggregated and thus the XRD underestimated the results.

For Pt/GrC, after 1,000 AST cycles, ECSA reduced 16.1% with an increase of Pt particle size of 44% (Fig. 5c). Comparing to Pt/HSAC, whose ECSA reduced 52.4% with a 68% increase of Pt particle size (Fig. 5b). More than 2 times higher ECSA loss (Fig. 2) but with only 50% greater particle size growth and similar Pt loss from XRF measurements (Fig. 7) for Pt/HSAC strongly suggested that a greater Pt detachment occurred on HSAC support during the AST cycles. During carbon corrosion, the growth of the detached nanoparticles being thus stopped. In addition, the overall better dispersion of the Pt/HSAC catalyst at BOL limited the coalescence of the Pt/HSAC vs. the Pt/GrC, where the Pt nanoparticles were in closer proximity at BOL. Furthermore, it is believed that the mainly graphitic nature of the GrC support resulted in a

higher mobility of the Pt nanoparticles [10], therefore making the coalescence, and not the detachment the major ECSA loss mechanism.

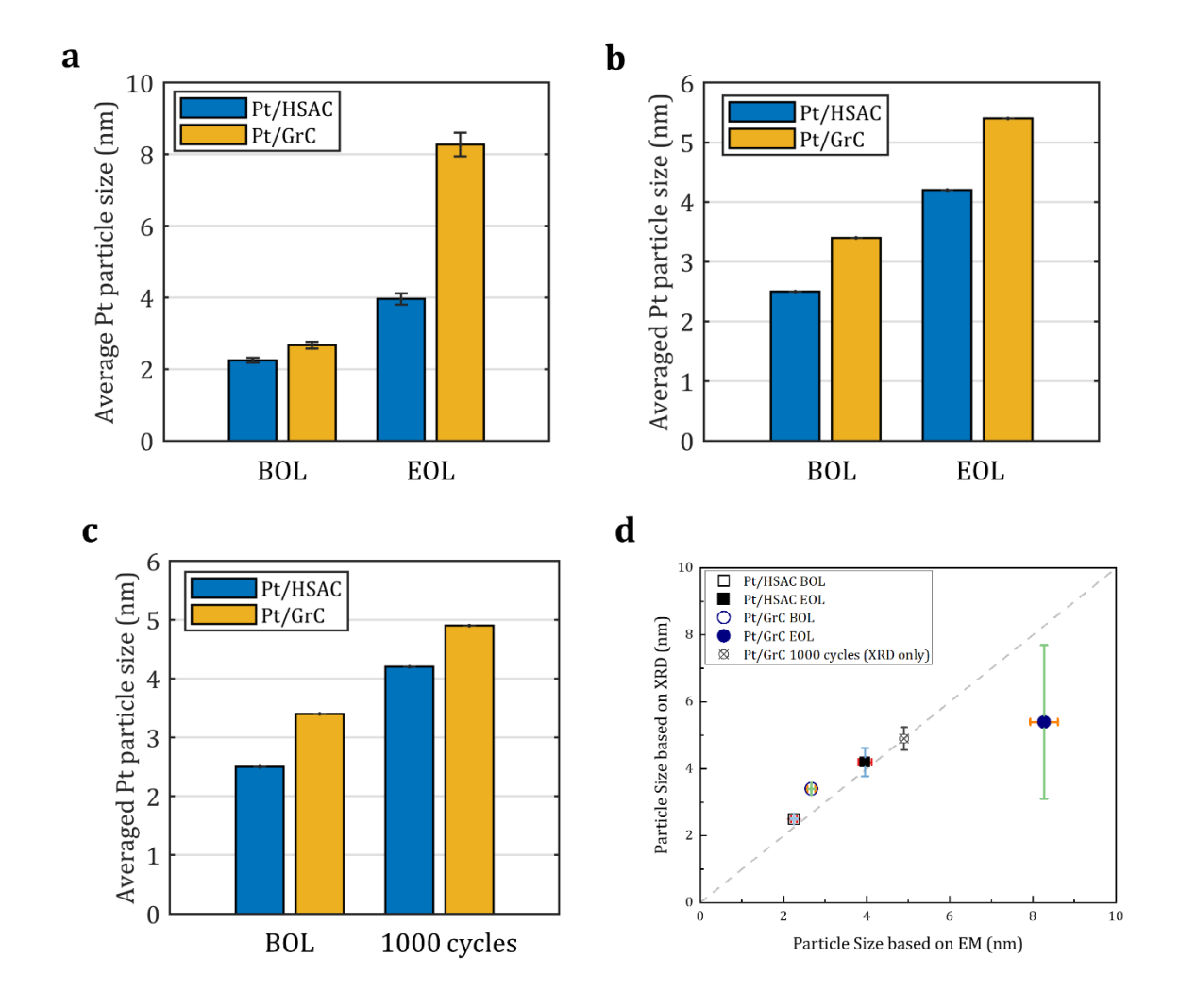


Fig. 5. Cathode Pt particle size measurement result using scanning transmission electron microscopy (STEM), transmission electron microscopy (TEM) and X-ray diffraction (XRD) for Pt/HSAC and Pt/GrC. (a) Scanning transmission electron micrographs of mean particles size at BOL and transmission electron micrographs of mean particles size at EOL, (b) X-ray diffraction of mean particles size at BOL and after 1,000 AST cycles (c) X-ray diffraction of mean particles size at BOL and Pt/GrC and (d) cathode Pt particle size determined from XRD as a function of Pt particle size determined from electron micrographs (EM). The dashed line represents a one-to-one correlation.

3.6. Cathode surface chemistry.

In this work, high-resolution XPS spectra was performed to study the cathode surface chemistry for both Pt/HSAC and Pt/GrC at BOL and EOL. Fig. S7 shows the relative percentages of different elements, surface carbonaceous moieties and surface Pt species before and after the AST. The curved fittings of high-resolution C *1s* spectra and the summarized quantitative results are shown in the Fig. S5 and Table. 1. The curved fittings for Pt *4f* spectra and the summarized quantitative results are shown in Fig. S6 and Table. 2.

The percentages of the sp^2 graphitic carbon peak for Pt/GrC and Pt/HSAC were different. For Pt/HSAC (Fig. S7b) after 1,000 AST cycles, no obvious change in the graphitic carbon concentration was observed (from 46.6% at BOL to 46.3% at EOL). However, for Pt/GrC (Fig. S7a) at EOL, concentration of graphitic carbon dropped from 56.3% to 46.1% on the surface after 10,000 AST cycles. The sp^3 carbon concentration corresponding to C-C increased for Pt/GrC after AST was accompanying with the decrease of the sp^2 graphitic carbon concentration might because of the degradation of graphitic carbon (probably happen at the edge). The changes in the total amount of carbon-oxygen groups (including C-O, C=O and COOH) can express the extent of the carbon corrosion. For Pt/GrC, the carbon-oxygen groups amount did not change much for the entire AST process. For Pt/HSAC, the total amount of the carbon-oxygen group increased from 18.4% to 24.1% at EOL (1,000 AST cycle). This indicates that the carbon support of the Pt/HSAC corroded after 1,000 AST cycles.

The ratio of CF₂ and CF can reveal the ionomer's morphology. For Pt/GrC, the ratio of CF₂/CF changed from 0.26 to 0.81 after 1,000 AST cycles, and then to 0.69 at EOL after 10,000 AST cycles. For Pt/HSAC, ratio of CF₂/CF changed from 0.15 to 0.83 after 1,000 AST cycles. This indicates that the ionomer rearranged in both cases. The C-F concentration reduction

usually correlates to the ionomer degradation. Here for Pt/HSAC, relative amount of C-F dropped from 20.3% to 11.0% after 1,000 AST cycles. However for the Pt/GrC, relative amount of C-F decreased from the 16.3% to 11.3% after 1,000 AST cycles, and then increased to 18.8% at EOL after 10,000 AST cycles due to the exposure of the hydrophilic C-F side chains of the ionomers.

Table. 1. Relative concentrations for surface C species for cathodes of Pt/HSAC and Pt/GrC before and after AST

(%)	Binding energy (eV)	g Pt/GrC BOL	Std.	Pt/GrC 1,000 cycles	Std.	Pt/GrC EOL	Std.	Pt/HSAG BOL	Std.	Pt/HSAG	Std.
sp^2	~284	56.3	1.87	56.2	0.68	46.1	1.47	46.6	1.52	46.3	1.25
C-C	~285	4.3	1.30	3.4	0.72	5.4	2.11	4.6	1.89	1.6	0.81
C*	~286	6.4	1.21	6.3	0.54	4.8	1.01	6.0	1.39	6.3	0.58
С-О	~287	3.7	1.05	3.9	0.35	2.9	0.95	5.2	0.98	4.7	0.70
C=O	~288	3.4	0.92	3.3	0.31	4.1	0.50	5.9	0.61	5.2	0.76
СООН	~289	3.7	1.11	3.3	0.26	3.2	1.11	7.3	1.59	14.2	1.42
C-F	~291	16.3	0.85	11.3	0.6	18.8	3.23	20.3	1.20	11.0	2.77
C-F ₂	~292	4.3	1.23	9.1	0.72	12.9	3.25	3.2	0.96	9.1	2.32
C-F ₃	~293	1.7	0.98	3.3	0.51	1.8	0.83	1.0	0.75	1.7	1.17

The Pt environment of the samples had been changed after the AST, as shown in Fig. S7c-d and Table. 2. For both samples, the relative concentration of metallic Pt increased while Pt-C decreased when compared the samples at BOL and EOL. This phenomenon is consistent with the Pt size

grew observed in the TEM and XRD. Pt species relative concentrations were similar when comparing Pt/GrC (Fig. S7c) to Pt/HSAC (Fig. S7d) at their EOLs (1,000 AST cycles for Pt/HSAC and 10,000 AST cycles for Pt/GrC). However, when comparing both samples after the 1,000 AST cycles, the relative concentrations of Pt species of Pt/GrC did not change as severely as the one of Pt/HSAC. This result also shows the consistency to the slight ECSA reduction for Pt/GrC after 1,000 AST cycles.

Table. 2. Relative concentrations for surface Pt species for cathodes of Pt/HSAC and Pt/GrC before and after AST

(%)	Binding energy (eV)	Pt/GrC BOL	Std.	Pt/GrC 1,000 cyc	Std.	Pt/GrC EOL	Std.	Pt/HSAC BOL	Std.	Pt/HSAC EOL	Std.
Pt ⁰	~70.9	53.2	3.09	57.1	1.54	65.2	3.86	49.3	3.79	63.3	3.12
Pt-C	~71.7	30.1	3.62	27.1	3.07	17.6	4.78	32.4	4.01	18.0	2.89
Pt-O	~73.3	16.7	2.01	15.8	2.61	17.2	3.78	18.3	2.66	18.7	3.57

3.7. Cathode carbon characterization.

Raman measurement was performed on cathode sides of both Pt/HSAC and Pt/GrC MEAs. The results for the range of 1,000 to 1800 cm⁻¹ are shown in Fig. S8. The D band (~1330 cm⁻¹) is related to the disordered carbon of the sample, while the G band (~1580 cm⁻¹) is related to the graphitic carbon. An additional D' band (~1614 cm⁻¹) appears when the disordered graphitic lattice exists [38,39]. The ratio of the intensities of the D band to the G band (D/G ratio) is shown in Table. 3. For the pristine samples, the D/G ratio of the Pt/HSAC (Fig. S8a) sample was higher, meaning that the carbon in Pt/HSAC sample was more disordered than the Pt/GrC sample. The G

band of the Pt/HSAC sample was shifted slightly since its graphitic carbon was highly disordered. Inversely, the D/G ratio of the Pt/GrC sample (Fig. S8b) was less than 1, meaning that the sample contained more graphitic carbon than the disordered one. Additionally, a clear D' band is shown in the spectra of the Pt/GrC sample since its G band was sharp. This sharp G band indicated that the Pt/GrC sample contained the graphitic carbon with higher degree of crystallinity [40]. After 1,000 AST cycles, the D/G ratio of Pt/HSAC (Fig. S8a) increased to 1.256, meaning that more disordered carbon appeared after the AST. Thus, the amorphous degree of the Pt/HSAC was getting higher. The D/G ratio of Pt/GrC after 1,000 AST cycles (Fig. S8b) reached to 1.156 with the sharp D' peak existing. When the Pt/GrC hits the EOL (10,000 AST cycles), the D/G ratio increased to 1.372. The G peak shifted to lower Raman shift and the dispersion increased. This is the sign of nanocrystalline graphite transformed to sp^2 amorphous carbon [39]. This phenomenon supports the conclusion gained from the XPS results, where the concentration of the graphitic carbon of the Pt/GrC decreased at its EOL. Considered the sp^3 carbon detected on the surface is way less than 30%, the carbon should be mainly at sp^2 amorphous status.

Table. 3. Cathode Raman D/G ratio of Pt/GrC and Pt/HSAC before and after AST

Sample	D/G ratio			
Pt/GrC BOL	0.980			
Pt/GrC after 1,000 AST cycles	1.156			
Pt/GrC after 10,000 AST cycles (EOL)	1.372			
Pt/HSAC BOL	1.081			
Pt/HSAC after 1,000 AST cycles (EOL)	1.256			

3.8. Cathode catalyst layer ionic conductivities and sulfonic acid group coverages

Cathode catalyst layer ionic conductivities were measured and shown in Fig. 6a by using a H₂/N₂ EIS fitting model according to Qi et al. [31] for both Pt/HSAC and Pt/GrC at their BOLs and EOLs. In that work, cell active area, frequency, real part of impedance, imaginary part of impedance and catalyst layer thickness were input into the developed H₂/N₂ EIS impedance fitting model and effective ionic conductivity was derived. For Pt/HSAC, the impedance Nyquist plots at BOL and EOL are shown in Fig. S9a and Fig. S9b, respectively, and an example impedance fitting at BOL and EOL using the 1D H₂/N₂ EIS fitting model are shown in Fig. S10a and Fig. S10b, respectively. According to the fitting results, cathode catalyst layer ionic conductivity decreased from 4.2×10^{-2} S cm⁻¹ at BOL to 1.97×10^{-2} S cm⁻¹ (53.1%) after 1,000 AST cycles at EOL. For Pt/GrC, the impedance Nyquist plots at BOL and EOL are shown in Fig. S9c and Fig. S9d, respectively, and an example impedance fitting at BOL and EOL using the 1D H₂/N₂ EIS fitting model are shown in Fig. S10c and Fig. S10d, respectively. Ionic conductivity of Pt/GrC cathode catalyst layer was 5.2x10⁻² S cm⁻¹ at BOL, which was higher compared to Pt/HSAC, since the graphitic carbon supports have better ionomer continuity and uniformity than disordered HSAC supports [41]. At EOL, catalyst ionic conductivity increased to 1.88x10⁻² S cm⁻¹. The reduction of ionic conductivity for both Pt/HSAC and Pt/GrC was due to the carbon corrosion leading to the further increase of discontinuity of ionomer and water distributions within the catalyst layer, causing higher tortuosity of H⁺ transport. Apart from that, Pt loss during the carbon corrosion resulted in worse continuity of ionic pathways with catalyst layer, leading to more tortuous H⁺ transport pathways.

Cathode SO₃ group coverages at 0.4 V for both Pt/HSAC and Pt/GrC were calculated and shown in Fig. 6b using CO displacement (Fig. S11a for Pt/HSAC and Fig. S11b for Pt/GrC) and CO stripping (Fig. S11c and Fig. S11d for Pt/HSAC and Fig. S11e and Fig. S11f for Pt/GrC) methods. For Pt/HSAC, SO₃ group coverage decreased from 13.8% at BOL to 6.8% after 1,000 AST cycles at EOL. According to the combined results of the ECSA loss, Pt loss and detachment leading to the ionomer detachment might be the principal reason for the 50.7% reduction of SO₃ group coverage at the EOL. Pt/GrC shows a higher SO₃ group coverage of 24.1% at BOL compared to Pt/HSAC because Pt particles within HSAC support mesopores were not in contact with ionomer. Recent studies showed that Pt nanoparticles within mesoporous carbon support are buried not too far into the pores but at the same time were not contacted by SO₃ groups [41–43]. Apart from that, Qi et al. [33] also showed that SO₃ group coverage was less dependent to Pt loading, but more dependent to carbon support type. After 10,000 AST cycles, SO₃ group coverage for Pt/GrC reached 6.39%, which again might be because ionomer detached Pt surface

caused by Pt loss and detachment.

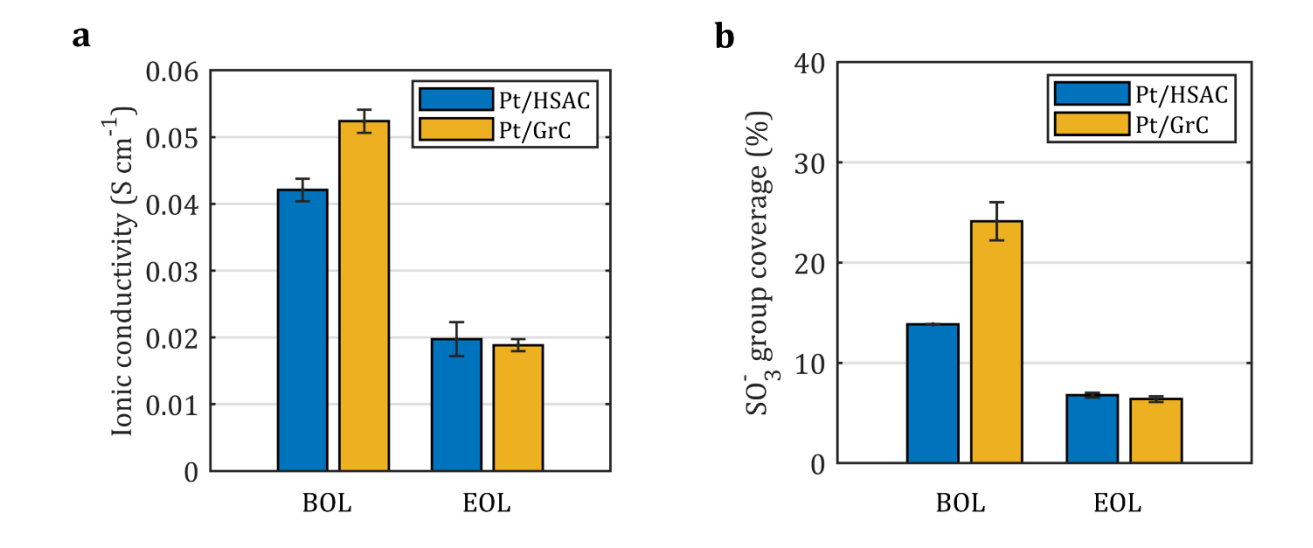


Fig. 6. (a) Cathode catalyst layer ionic conductivity reduction for and (b) cathode catalyst layer SO₃ group coverage for Pt/HSAC and Pt/GrC at BOL and EOL.

4. Discussion: in-situ and ex-situ characterizations comparison between Pt/HSAC and Pt/GrC after 1,000 AST cycles

An additional MEA using GrC support was subjected to study both in-situ and ex-situ electrochemical characterizations after 1,000 AST cycles. Then a further detailed comparison was published and shown in Fig. 8 between Pt/HSAC and Pt/GrC to investigate the different levels of degradations of different carbon supports after same AST cycles. Fig. 8a compares the MEA performance and HFR results between Pt/HSAC and Pt/GrC at BOL and after 1,000 AST cycles. Pt/HSAC experienced a rapid cell performance deterioration after 1,000 AST cycles while a much more moderate voltage drop of 14 mV at 1 A cm⁻² was found for Pt/GrC. Apart from that, after 1,000 AST cycles, HFR for Pt/GrC decreased from 52.8 mohms cm² to 50.8 mohms cm² due to better interfacial contacts between components and further cell hydration. However, HFR for Pt/HSAC increased from 56.4 mohms cm² to 73.3 mohms cm² because of

thickness reduction of catalyst layer, which is shown in Fig. 2. Fig. 8b shows the cathode ECSA comparison. After 1,000 AST cycles, ECSA of Pt/HSAC decreased from 43.5 m² g⁻¹ to 20.7 m² g⁻¹ (52.4%). For Pt/GrC, ECSA decreased from 26.2 m² g⁻¹ to 22 m² g⁻¹ (16.1%) after 1,000 AST cycles, which is much less compared to Pt/HSAC. Catalyst layer thickness comparison is shown in Fig. 8c. Cathode catalyst layer thickness for Pt/HSAC reduced by 7.7 μm (67.5%) after 1,000 AST cycles. However according to SEM measurement results shown in Fig. S12, cathode catalyst layer thickness reduced from 18.7 μm to 14.6 μm (21.9%) after 1,000 AST cycles, which again indicates that Pt/GrC was much more robust compared to Pt/HSAC. Fig. 7c shows that cumulative average Pt loading of Pt/HSAC reached 0.675 mg cm⁻² at the BOL (Fig. 7a) and decreased to 0.577 mg cm⁻² after 1,000 AST cycles (Fig. 7b). For Pt/GrC, cumulative averaged Pt loading shown in Fig. 7f decreased from 0.750 mg cm⁻² at BOL (Fig. 7d) to 0.628 mg cm⁻² after 1,000 AST cycles (Fig. 7e). Again, more than 2 times higher ECSA loss (Fig. 8b) but with only 50% greater particle size growth and similar Pt loss from XRF

measurements (Fig. 7) for Pt/HSAC strongly suggested that a greater Pt detachment occurred on HSAC support during the AST cycles.

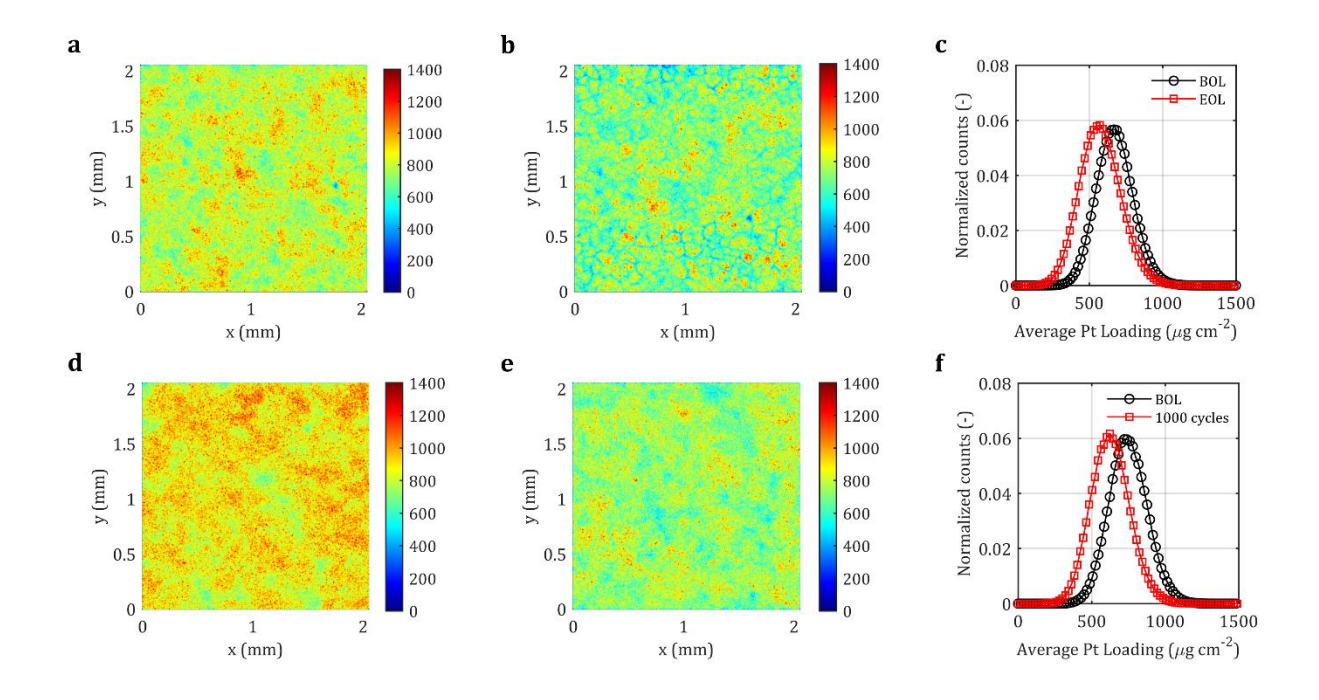


Fig. 7. Identical location micro X-ray fluorescence (XRF) maps for Pt/HSAC at (a) BOL and (b) after 1,000 AST cycles. (c) Loading-frequency distribution for Pt/HSAC at BOL and after 1,000 AST cycles. Identical location micro X-ray fluorescence (micro XRF) maps for Pt/GrC at (d) BOL and (e) after 1,000 AST cycles. (f) Loading-frequency distribution for Pt/GrC at BOL and after 1,000 AST cycles.

Fig. 8d compares the cathode catalyst layer ionic conductivity between Pt/HSAC and Pt/GrC at BOL and after 1,000 AST cycles according to Fig. S9a-b, Fig. S10a-b and Fig. S13a-d. For Pt/HSAC, catalyst layer ionic conductivity decreased by 53.1% after 1,000 AST cycles at EOL. However, for Pt/GrC, the decrease of catalyst layer ionic conductivity was around 2.5 times smaller compared to Pt/HSAC, which was 21.9% after 1,000 AST cycles. According to the comparisons of CO displacement and CO stripping measurements shown in Fig. S11(a,c,d) and

Fig. S13e-f, cathode SO₃ group coverage comparison at 0.4 V for both Pt/HSAC and Pt/GrC at BOL and after 1,000 AST cycles were calculated and shown in Fig. 8e). SO₃ group coverage decreased by 50.9% for Pt/HSAC, compared to 11.8% for Pt/HSAC, which was around 4 times smaller.

This comprehensive work again proves that MEAs containing low surface area carbon support are more robust. Macauley et al. [10] also showed that graphitized carbon support had 9 times lower carbon corrosion rate compared to HSAC support.

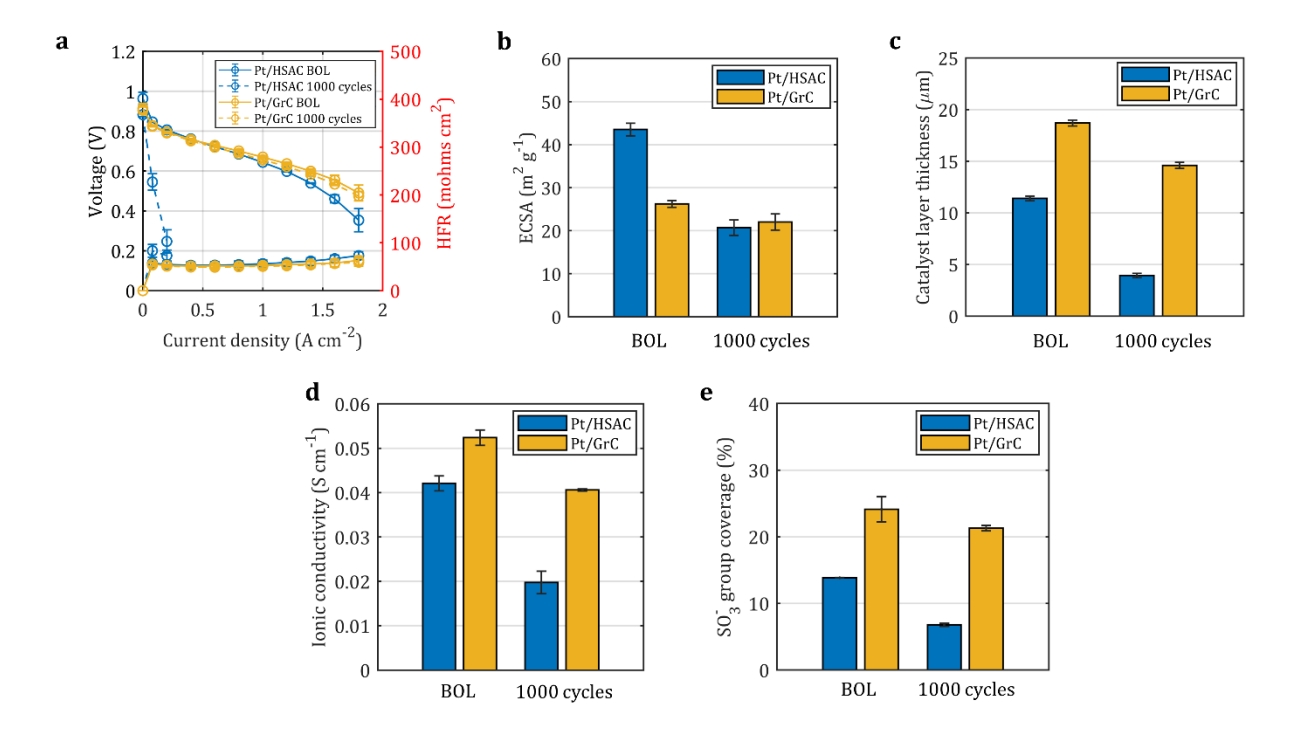


Fig. 8. Electrochemical characterizations and ex-situ measurements comparison between Pt/HSC and Pt/GrC at BOL and after 1,000 AST cycles. (a) MEA performance and HFRs at 80 °C, 100% RH, 150 kPa in H₂/Air with stoichiometric anode and cathode flows of 2 and 2, (b) cathode ECSA, (c) cathode catalyst layer thickness, (d) cathode catalyst layer ionic conductivity and (e) cathode catalyst layer SO₃ group coverage.

5. Conclusion.

PEFC MEAs custom-made by IRD Fuel Cells with HSAC and GrC supports were subjected to the carbon corrosion AST published by the U.S. DRIVE FCTT. In this work, spectroscopic techniques were performed and the performance changes after ASTs were measured. 1,000 AST cycles were conducted on Pt/HSAC and 10,000 AST cycles were conducted on Pt/GrC due to different carbon corrosion rates. Polarization curve results showed that Pt/GrC did not meet DOE target of 40 mV loss at 0.8 A cm⁻² and 40 mV loss at 1.5 A cm⁻² after 5000 AST cycles. Carbon corroded during the AST and formed rougher carbon surfaces and created more contacts with ionomer and water, which resulted in increases of C_{dl} for Pt/HSAC (7.5%) and Pt/GrC (69.8%) at their EOLs. The Pt/GrC support was more ordered and organized, however after AST, a nonnegligible fraction of disordered carbon was generated, leading to a more significant increase of C_{dl}. ECSA was lost during AST for both Pt/HSAC and Pt/GrC because of Pt loss, Pt detachment from the carbon support and Pt particle size growth. Cumulative Pt loading decreased 14.5% and 8.3% for Pt/HSAC and Pt/GrC after AST at their EOLs, respectively. For Pt/HSAC, Pt detachment might be one of the major reasons leading to the 52.4% reduction of ECSA. However for Pt/GrC, after 5000 AST cycles, a ECSA loss of 30.6% was observed, which met the DOE target of less than 40% ECSA loss compared to the BOL. After 10,000 AST cycles, the increase of particle size and Pt loss caused 44% loss of ECSA at the EOL. After 1,000 AST cycles at EOL, for Pt/HSAC, catalyst layer thickness reduced by 67.5% leading to a 30% increase of HFR due to insufficient contacts between GDL and catalyst layer. For Pt/GrC after 10,000 AST cycles, a catalyst layer thickness reduction of 68.4% was observed whereas the HFR almost remained unchanged due to sufficient contacts between GDL and catalyst layer after AST. After AST, both Pt/HSAC and Pt/GrC showed higher D/G ratio from Raman measurements, meaning that the carbon status became more disordered. Cathode catalyst layer ionic conductivity for Pt/HSAC and Pt/GrC

decreased 53.1% and 63.8% after AST at their EOLs, and it was found that the SO₃ group coverage decreased 50.7% and 73.5% for Pt/HSC and Pt/GrC, respectively. An in-situ and ex-situ electrochemical characterizations comparison between Pt/HSAC and Pt/GrC after 1,000 AST cycles was displayed. Graphitized carbon support was much more robust compared to HSAC support, and it showed 2 times less ECSA reduction, 2.5 times less catalyst layer ionic conductivity reduction and 4 times less SO₃ group coverage drop.

Acknowledgement

The authors acknowledge funding from the National Science Foundation CAREER award 1652445. The authors acknowledge the use of facilities and instrumentation at the UC Irvine Materials Research Institute (IMRI). XPS work was performed using instrumentation funded in part by the National Science Foundation Major Research Instrumentation Program under grant no. CHE-1338173. The XRF and Raman work was done at the HIMaC²'s Analytical Laboratory, a user facility operated by the Horiba Institute for Mobility and Connectivity, University California, Irvine.

References

- [1] Y. Manoharan, S.E. Hosseini, B. Butler, H. Alzhahrani, B.T.F. Senior, T. Ashuri, J. Krohn, Hydrogen fuel cell vehicles; Current status and future prospect, Appl. Sci. 9 (2019) 2296. https://doi.org/10.3390/app9112296.
- [2] J. Kast, R. Vijayagopal, J.J. Gangloff, J. Marcinkoski, Clean commercial transportation: Medium and heavy duty fuel cell electric trucks, Int. J. Hydrogen Energy. 42 (2017) 4508–4517. https://doi.org/10.1016/j.ijhydene.2016.12.129.

- [3] X. Liu, K. Reddi, A. Elgowainy, H. Lohse-Busch, M. Wang, N. Rustagi, Comparison of well-to-wheels energy use and emissions of a hydrogen fuel cell electric vehicle relative to a conventional gasoline-powered internal combustion engine vehicle, Int. J. Hydrogen Energy. 45 (2020) 972–983. https://doi.org/10.1016/j.ijhydene.2019.10.192.
- [4] S.G. Chalk, J.F. Miller, Key challenges and recent progress in batteries, fuel cells, and hydrogen storage for clean energy systems, J. Power Sources. 159 (2006) 73–80. https://doi.org/10.1016/j.jpowsour.2006.04.058.
- [5] M.S. Wilson, F.H. Garzon, K.E. Sickafus, S. Gottesfeld, Surface Area Loss of Supported Platinum in Polymer Electrolyte Fuel Cells, J. Electrochem. Soc. 140 (1993) 2872–2877. https://doi.org/10.1149/1.2220925.
- [6] A. Taniguchi, T. Akita, K. Yasuda, Y. Miyazaki, Analysis of electrocatalyst degradation in PEMFC caused by cell reversal during fuel starvation, J. Power Sources. 130 (2004) 42–49. https://doi.org/10.1016/j.jpowsour.2003.12.035.
- [7] T.F. Cells, F. Cell, T. Office, F. Cells, T. Office, T.F. Cells, Fuel Cell 2016 Multi-Year Research, Development, and Demonstration Plan, 2015 (2016) 1–58.
- [8] R. Borup, A. Weber, FC135: FC-PAD: Fuel Cell Performance and Durability

 Consortium, 2019 DOE Fuel Cell Technol. Off. Annu. Merit Rev. 1 (2020) 1–42.
- [9] R. Borup, J. Meyers, B. Pivovar, Y.S. Kim, R. Mukundan, N. Garland, D. Myers, M. Wilson, F. Garzon, D. Wood, P. Zelenay, K. More, K. Stroh, T. Zawodzinski, J. Boncella, J.E. McGrath, M. Inaba, K. Miyatake, M. Hori, K. Ota, Z. Ogumi, S. Miyata, A. Nishikata, Z. Siroma, Y. Uchimoto, K. Yasuda, K.I. Kimijima, N. Iwashita, Scientific aspects of polymer electrolyte fuel cell durability and degradation, Chem. Rev. 107 (2007) 3904–3951. https://doi.org/10.1021/cr0501821.

- [10] N. Macauley, D.D. Papadias, J. Fairweather, D. Spernjak, D. Langlois, R. Ahluwalia, K.L. More, R. Mukundan, R.L. Borup, Carbon Corrosion in PEM Fuel Cells and the Development of Accelerated Stress Tests, J. Electrochem. Soc. 165 (2018) F3148–F3160. https://doi.org/10.1149/2.0061806jes.
- [11] Q. Shen, M. Hou, D. Liang, Z. Zhou, X. Li, Z. Shao, B. Yi, Study on the processes of start-up and shutdown in proton exchange membrane fuel cells, J. Power Sources. 189 (2009) 1114–1119. https://doi.org/10.1016/j.jpowsour.2008.12.075.
- [12] E. Brightman, G. Hinds, In situ mapping of potential transients during start-up and shut-down of a polymer electrolyte membrane fuel cell, J. Power Sources. 267 (2014) 160–170. https://doi.org/10.1016/j.jpowsour.2014.05.040.
- [13] P. Mandal, B.K. Hong, J.G. Oh, S. Litster, Understanding the voltage reversal behavior of automotive fuel cells, J. Power Sources. 397 (2018) 397–404. https://doi.org/10.1016/j.jpowsour.2018.06.083.
- [14] N. Garland, T. Benjamin, DOE Fuel Cell Program: Durability Technical Targets and Testing Protocols, ECS Meet. Abstr. MA2007-02 (2007) 589–589. https://doi.org/10.1149/ma2007-02/9/589.
- [15] N.G. Author, Fuel Cell Technical Team Roadmap, (2013). https://doi.org/10.2172/1220127.
- [16] L. Castanheira, W.O. Silva, F.H.B. Lima, A. Crisci, L. Dubau, F. Maillard, Carbon corrosion in proton-exchange membrane fuel cells: Effect of the carbon structure, the degradation protocol, and the gas atmosphere, ACS Catal. 5 (2015) 2184–2194. https://doi.org/10.1021/cs501973j.

- [17] K. Miyazaki, H. Shirakata, T. Abe, N. Yoshizawa, Z. Ogumi, Novel graphitised carbonaceous materials for use as a highly corrosion-tolerant catalyst support in polymer electrolyte fuel cells, Fuel Cells. 10 (2010) 960–965. https://doi.org/10.1002/fuce.2010,00075.
- [18] H.S. Oh, K.H. Lim, B. Roh, I. Hwang, H. Kim, Corrosion resistance and sintering effect of carbon supports in polymer electrolyte membrane fuel cells, Electrochim. Acta. 54 (2009) 6515–6521. https://doi.org/10.1016/j.electacta.2009.06.028.
- [19] S. Vinod Selvaganesh, G. Selvarani, P. Sridhar, S. Pitchumani, A.K. Shukla, Graphitic carbon as durable cathode-catalyst support for PEFCs, Fuel Cells. 11 (2011) 372–384. https://doi.org/10.1002/fuce.201,000151.
- [20] S. Maass, F. Finsterwalder, G. Frank, R. Hartmann, C. Merten, Carbon support oxidation in PEM fuel cell cathodes, J. Power Sources. 176 (2008) 444–451. https://doi.org/10.1016/j.jpowsour.2007.08.053.
- [21] N. Linse, L. Gubler, G.G. Scherer, A. Wokaun, The effect of platinum on carbon corrosion behavior in polymer electrolyte fuel cells, Electrochim. Acta. 56 (2011) 7541–7549. https://doi.org/10.1016/j.electacta.2011.06.093.
- [22] T. Mittermeier, A. Weiß, F. Hasché, H.A. Gasteiger, PEM Fuel Cell Start-Up/Shut-Down Losses vs Relative Humidity: The Impact of Water in the Electrode Layer on Carbon Corrosion, J. Electrochem. Soc. 165 (2018) F1349–F1357.

 https://doi.org/10.1149/2.0931816jes.
- [23] A.G. Star, T.F. Fuller, FIB-SEM Tomography Connects Microstructure to Corrosion-Induced Performance Loss in PEMFC Cathodes, J. Electrochem. Soc. 164 (2017) F901–F907. https://doi.org/10.1149/2.0321709jes.

- [24] F. Hegge, J. Sharman, R. Moroni, S. Thiele, R. Zengerle, M. Breitwieser, S. Vierrath, Impact of Carbon Support Corrosion on Performance Losses in Polymer Electrolyte Membrane Fuel Cells, J. Electrochem. Soc. 166 (2019) F956–F962. https://doi.org/10.1149/2.0611913jes.
- [25] P. Saha, K. Khedekar, H. Wang, P. Atanassov, L. Cheng, S. Stewart, C. Johnston, I. V. Zenyuk, Correlating the morphological changes to electrochemical performance during carbon corrosion in polymer electrolyte fuel cells, J. Mater. Chem. A. (2022) 12551–12562. https://doi.org/10.1039/d2ta02666j.
- [26] S. Kabir, D.J. Myers, N. Kariuki, J. Park, G. Wang, A. Baker, N. Macauley, R. Mukundan, K.L. More, K.C. Neyerlin, Elucidating the Dynamic Nature of Fuel Cell Electrodes as a Function of Conditioning: An ex Situ Material Characterization and in Situ Electrochemical Diagnostic Study, ACS Appl. Mater. Interfaces. (2019). https://doi.org/10.1021/acsami.9b11365.
- [27] J. Schindelin, I. Arganda-Carreras, E. Frise, V. Kaynig, M. Longair, T. Pietzsch, S. Preibisch, C. Rueden, S. Saalfeld, B. Schmid, J.Y. Tinevez, D.J. White, V. Hartenstein, K. Eliceiri, P. Tomancak, A. Cardona, Fiji: An open-source platform for biological-image analysis, Nat. Methods. 9 (2012) 676–682. https://doi.org/10.1038/nmeth.2019.
- [28] K. Artyushkova, P. Atanassov, M. Dutta, S. Wessel, V. Colbow, Structural correlations: Design levers for performance and durability of catalyst layers, J. Power Sources. 284 (2015) 631–641. https://doi.org/10.1016/j.jpowsour.2015.02.135.
- [29] A. Patel, K. Artyushkova, P. Atanassov, V. Colbow, M. Dutta, D. Harvey, S. Wessel, Investigating the effects of proton exchange membrane fuel cell conditions on carbon

- supported platinum electrocatalyst composition and performance, J. Vac. Sci. Technol. A Vacuum, Surfaces, Film. 30 (2012) 04D107. https://doi.org/10.1116/1.4707153.
- [30] H. Iden, A. Ohma, An in situ technique for analyzing ionomer coverage in catalyst layers, J. Electroanal. Chem. 693 (2013) 34–41. https://doi.org/10.1016/j.jelechem.2013.01.026.
- [31] Y. Qi, J. Liu, D.C. Sabarirajan, Y. Huang, A. Perego, A.T. Haug, I. V. Zenyuk,
 Interpreting Ionic Conductivity for Polymer Electrolyte Fuel Cell Catalyst Layers with
 Electrochemical Impedance Spectroscopy and Transmission Line Modeling, J.
 Electrochem. Soc. 168 (2021) 054502. https://doi.org/10.1149/1945-7111/abf96d.
- [32] M. Obermaier, A.S. Bandarenka, C. Lohri-Tymozhynsky, A Comprehensive Physical Impedance Model of Polymer Electrolyte Fuel Cell Cathodes in Oxygen-free Atmosphere, Sci. Rep. 8 (2018) 1–9. https://doi.org/10.1038/s41598-018-23071-5.
- [33] Y. Qi, Y. Morimoto, M.S. Shibata, Z. Gao, D.C. Sabarirajan, A.T. Haug, I. V. Zenyuk,
 Understanding Platinum Ionomer Interface Properties of Polymer Electrolyte Fuel Cells, J.
 Electrochem. Soc. 169 (2022) 064512. https://doi.org/10.1149/1945-7111/ac774f.
- [34] T.R. Garrick, T.E. Moylan, V. Yarlagadda, A. Kongkanand, Characterizing Electrolyte and Platinum Interface in PEM Fuel Cells Using CO Displacement, J. Electrochem. Soc. 164 (2017) F60–F64. https://doi.org/10.1149/2.0551702jes.
- [35] F. Maillard, M. Eikerling, O. V. Cherstiouk, S. Schreier, E. Savinova, U. Stimming, Size effects on reactivity of Pt nanoparticles in CO monolayer oxidation: The role of surface mobility, Faraday Discuss. 125 (2004) 357–377. https://doi.org/10.1039/b303911k.
- [36] T. Binninger, E. Fabbri, R. Kötz, T.J. Schmidt, Determination of the Electrochemically Active Surface Area of Metal-Oxide Supported Platinum Catalyst, J. Electrochem. Soc. 161 (2014) H121–H128. https://doi.org/10.1149/2.055403jes.

- [37] C.R. Adams, H.A. Benesi, R.M. Curtis, R.G. Meisenheimer, Particle size determination of supported catalytic metals: Platinum on silica gel, J. Catal. 1 (1962) 336–344. https://doi.org/10.1016/0021-9517(62)90061-1.
- [38] A. Sadezky, H. Muckenhuber, H. Grothe, R. Niessner, U. Pöschl, Raman microspectroscopy of soot and related carbonaceous materials: Spectral analysis and structural information, Carbon N. Y. 43 (2005) 1731–1742. https://doi.org/10.1016/j.carbon.2005.02.018.
- [39] A.C. Ferrari, Raman spectroscopy of graphene and graphite: Disorder, electron-phonon coupling, doping and nonadiabatic effects, Solid State Commun. 143 (2007) 47–57. https://doi.org/10.1016/j.ssc.2007.03.052.
- [40] M. Sahoo, B.P. Vinayan, S. Ramaprabhu, Platinum-decorated chemically modified reduced graphene oxide-multiwalled carbon nanotube sandwich composite as cathode catalyst for a proton exchange membrane fuel cell, RSC Adv. 4 (2014) 26140–26148. https://doi.org/10.1039/c4ra02542c.
- [41] N. Ramaswamy, W. Gu, J.M. Ziegelbauer, S. Kumaraguru, Carbon Support Microstructure Impact on High Current Density Transport Resistances in PEMFC Cathode, J. Electrochem. Soc. 167 (2020) 064515. https://doi.org/10.1149/1945-7111/ab819c.
- [42] J.K. Clark, S.J. Paddison, Side chain flexibility in perfluorosulfonic acid ionomers: An Ab initio study, J. Phys. Chem. A. 117 (2013) 10534–10543.
 https://doi.org/10.1021/jp407568d.
- [43] S. Ott, A. Orfanidi, H. Schmies, B. Anke, H.N. Nong, J. Hübner, U. Gernert, M. Gliech,M. Lerch, P. Strasser, Ionomer distribution control in porous carbon-supported catalyst

layers for high-power and low Pt-loaded proton exchange membrane fuel cells, Nat.

Mater. 19 (2020) 77–85. https://doi.org/10.1038/s41563-019-0487-0.